

**Influence of compressibility on the Lagrangian statistics of vorticity–strain-rate interactions**Mohammad Danish,<sup>\*</sup> Sawan Suman Sinha,<sup>†</sup> and Balaji Srinivasan<sup>‡</sup>*Department of Applied Mechanics, Indian Institute of Technology Delhi, New Delhi 110016, India*

(Received 9 March 2016; revised manuscript received 23 May 2016; published 6 July 2016)

The objective of this study is to investigate the influence of compressibility on Lagrangian statistics of vorticity and strain-rate interactions. The Lagrangian statistics are extracted from “almost” time-continuous data sets of direct numerical simulations of compressible decaying isotropic turbulence by employing a cubic spline-based Lagrangian particle tracker. We study the influence of compressibility on Lagrangian statistics of alignment in terms of compressibility parameters—turbulent Mach number, normalized dilatation-rate, and flow topology. In comparison to incompressible turbulence, we observe that the presence of compressibility in a flow field weakens the alignment tendency of vorticity toward the largest strain-rate eigenvector. Based on the Lagrangian statistics of alignment conditioned on dilatation and topology, we find that the weakened tendency of alignment observed in compressible turbulence is because of a special group of fluid particles that have an initially negligible dilatation-rate and are associated with stable-focus-stretching topology.

DOI: [10.1103/PhysRevE.94.013101](https://doi.org/10.1103/PhysRevE.94.013101)**I. INTRODUCTION**

Concurrence of several linear and nonlinear processes (production, cascade, mixing, material element deformation, intermittency, etc.) combined with the presence of a wide spectrum of time and length scales makes turbulence a challenging problem to analyze and comprehend. A key quantity whose dynamics encodes many of turbulence processes is the small-scale velocity gradient tensor [1]. In the past three decades, several studies have been performed to enhance our understanding of the dynamics of velocity gradient and its evolution in homogeneous turbulence [2–10].

Broadly, the dynamics of the velocity gradient tensor can be studied either within an Eulerian or a Lagrangian framework. The former approach is more popular because of the simplicity in measuring as well computing an Eulerian flow field. However, the latter approach offers a useful complementary point of view to develop deeper insights into the historical evolution of various turbulence processes in a flow field following a fluid particle [11–13]. Specifically, a Lagrangian perspective is highly desirable to develop improved closure models for the Lagrangian stochastic methods of turbulence computations [14,15]. For example, the restricted Euler equation [16–22] and the homogenized Euler equation [23–25] are two available closure models that attempt to capture the Lagrangian evolution of velocity gradients in a turbulent flow field. Thus, an improved understanding of the dynamics of turbulent velocity gradients, employing either experimental or numerical measurements in a Lagrangian framework, has the potential to directly contribute toward further improvement of such closure models [1].

An extensive study on the Lagrangian statistics of velocity, acceleration, dissipation, etc. is presented by Yeung and Pope [26]. The Lagrangian data were obtained from direct numerical simulation (DNS) of incompressible forced isotropic turbulence at Taylor-microscale Reynolds number

( $Re_\lambda$ ) in the range  $38 \sim 92$ . The authors [26] observed a strong dependence of Reynolds number on the Lagrangian statistics as compared to their Eulerian counterparts. Later, these findings were confirmed by Yeung [27] at relatively higher Reynolds number as well ( $Re_\lambda \sim 234$ ). Yu and Meneveau [28] presented Lagrangian time-correlation functions for velocity gradient, strain-rate, and rotation-rate tensors. The authors [28] demonstrated that the correlation function of strain-rate decays very quickly, whereas the correlation function of rotation-rate tensor decorrelates relatively slowly. On the other hand, the correlation function of velocity gradient tensor lies between the correlation functions of strain-rate and rotation-rate tensors. A slow decorrelation of rotation-rate tensor is attributed to its association with vorticity, which is known for its long-lived structure [29]. Note that all these studies were performed for incompressible turbulence.

Experimental measurement of Lagrangian statistics has proven to be more challenging than the numerical approach. This is primarily because of the intermittent nature of particle acceleration [30], which results in particles to experience huge acceleration or deceleration over a very short span of time. However, recently, some important progress has been in this direction. For example, Ott and Mann [31] presented a study on turbulent diffusion for a pair of particles. La Porta *et al.* [30] presented probability distribution function (pdf) of acceleration variance at  $Re_\lambda = 200, 690, \text{ and } 970$ . The autocorrelation functions of acceleration from similar experiments were reported by Voth *et al.* [32]. The authors [32] found the Kolmogorov scaling for acceleration autocorrelation. Lüthi *et al.* [8] measured the full set of velocity gradient tensor using three-dimensional particle-tracking velocimetry. Many known results of DNS, such as positive skewness of intermediate eigenvalue of strain-rate and predominance of vortex stretching, were successfully reproduced. More recently, Xu *et al.* [33] have shed new light on the alignment tendency of vorticity with the strain-rate eigenvector. The authors [33] showed that the vorticity has a strong tendency to orient itself along the initially largest eigenvector of strain-rate. However, this process is not instantaneous but happens over a time delay of the order of the Kolmogorov timescale. The authors [33] call the tendency of the vorticity vector to align

<sup>\*</sup>mddanish.me@gmail.com<sup>†</sup>sawan@am.iitd.ac.in<sup>‡</sup>balaji@am.iitd.ac.in

with the largest strain-rate eigenvector as pirouette effect of turbulence. Thus, along with numerical results, the parallel progress in Lagrangian experiments has laid a wide scope for a better understanding of turbulence.

Recently, some Lagrangian studies [34–37] of compressible turbulence have also been presented. These studies have provided useful information regarding the particle distribution, structure functions, acceleration statistics, etc. We extend the study of Lagrangian study of compressible turbulence in terms of the velocity gradient tensor. However, unlike incompressible turbulence, the statistics of compressible turbulence needs to be parametrized on appropriate compressibility parameters. These compressibility parameters could be global or local. The turbulent Mach number and the ratio of dilatational to solenoidal kinetic energy are examples of global parameters, whereas dilatation-rate, growth-rate of dilatation, flow topology are examples of local compressibility parameters.

A global compressibility parameter may be useful to parametrize compressibility, if our interest lies in understanding the behavior of globally averaged velocity and pressure fields. If we intend to understand dynamics following a given particle, the global compressibility parameter like turbulent Mach number may not be the ideal way to parametrize compressibility. Several recent studies even on single-time statistics of compressible turbulence have reached to similar conclusion [9,10,24,38]—while the unconditioned globally averaged statistics may not show direct influence of a global compressibility parameter like turbulent Mach number, conditionally averaged statistics of pressure Hessian and velocity gradient tensor show profound effect of local compressibility parameters like normalized dilatation and rate of change of dilatation. It is these perceivable effects that gives us an opportunity to understand the mechanisms by which compressibility affects turbulence in a fundamental manner—not clouded by indiscriminate global averaging. Thus, for improving our understanding of compressibility on fluid dynamics in general and turbulence in particular, investigations conditioned upon local compressibility parameter seems essential.

The overarching goal of the present work is to identify and investigate the influence of compressibility on Lagrangian statistics of velocity gradients in compressible turbulence. Toward this goal, we employ direct numerical simulation results of compressible decaying isotropic turbulence over a range of turbulent Mach number. Relevant Lagrangian statistics is extracted from Eulerian databases employing a spline-based Lagrangian particle tracker (LPT) algorithm. In the present work, compressibility is parameterized in terms of turbulent Mach number, normalized dilatation-rate, and flow topology. We specifically focus on the influence of compressibility parameters on the so-called pirouette effect of turbulence. To clearly bring out the differences between compressible and incompressible turbulence, we contrast the results from compressible decaying turbulence with that in incompressible decaying turbulence.

The paper is organized in eight sections. In Sec. II, we present an overview of governing equations of the velocity gradient and pressure Hessian tensors in compressible turbulence. Here, we also present the quantities of interest and identify various compressibility parameters. In Sec. III, we present a description of the DNS employed for the present

study. A brief review of LPT algorithm and its validation are presented in Sec. IV. In Sec. V, we investigate the influence of turbulent Mach number on the pirouette effect of turbulence. Subsequently, in Sec. VI, the pirouette effects conditioned on topology and normalized dilatation rate are presented. The implications of the present work on Lagrangian models of velocity gradient are presented in Sec. VII. Finally, Sec. VIII ends the paper with a brief summary.

## II. DYNAMICS OF VELOCITY GRADIENTS

We start with conservation of mass, Newton’s second law of motion, and conservation of energy equations for a perfect gas:

$$\frac{\partial \rho}{\partial t} + V_k \frac{\partial \rho}{\partial X_k} = -\rho \frac{\partial V_k}{\partial X_k}, \quad (1)$$

$$\frac{\partial V_i}{\partial t} + V_k \frac{\partial V_i}{\partial X_k} = -\frac{1}{\rho} \frac{\partial p}{\partial X_i} + \frac{1}{\rho} \frac{\partial \sigma_{ik}}{\partial X_k}, \quad (2)$$

$$\begin{aligned} \frac{\partial T}{\partial t} + V_k \frac{\partial T}{\partial X_k} = & -T(n-1) \frac{\partial V_i}{\partial X_i} - \frac{n-1}{\rho R} \frac{\partial q_k}{\partial X_k} \\ & + \frac{n-1}{\rho R} \frac{\partial}{\partial X_j} (V_i \sigma_{ji}), \end{aligned} \quad (3)$$

where  $V_i$ ,  $\rho$ ,  $p$ ,  $T$ ,  $R$ ,  $\sigma_{ik}$ ,  $q_k$ ,  $n$  denote velocity, density, pressure, temperature, gas constant, stress tensor, heat flux, and ratio of specific heat values, respectively. The three thermodynamic variables  $\rho$ ,  $T$ , and  $p$  are related through the state equation

$$p = \rho RT. \quad (4)$$

The viscous stress tensor ( $\sigma_{ij}$ ) and the heat flux vector ( $q_k$ ) obey the following constitutive relationships:

$$\sigma_{ij} \equiv \mu \left( \frac{\partial V_i}{\partial X_j} + \frac{\partial V_j}{\partial X_i} \right) + \delta_{ij} \lambda \frac{\partial V_k}{\partial X_k}, \quad \text{and} \quad (5)$$

$$q_k \equiv -K \frac{\partial T}{\partial X_k}, \quad (6)$$

where  $\delta_{ij}$  is Kronecker  $\delta$ ,  $\mu$  and  $\lambda$  denote the first and second coefficients of viscosity, and  $K$  represents the thermal conductivity. Note that  $\lambda$  is taken as  $-\frac{2\mu}{3}$ .

Evolution equation of the velocity gradient tensor ( $A_{ij} = \partial V_i / \partial X_j$ ) is obtained by taking gradient of Eq. (2):

$$\begin{aligned} \frac{dA_{ij}}{dt} = & -A_{ik} A_{kj} - \underbrace{\frac{\partial}{\partial X_j} \left( \frac{1}{\rho} \frac{\partial p}{\partial X_i} \right)}_{P_{ij}} \\ & + \underbrace{\frac{\partial}{\partial X_j} \left\{ \frac{1}{\rho} \frac{\partial}{\partial X_k} \left[ \mu \left( \frac{\partial V_i}{\partial X_k} + \frac{\partial V_k}{\partial X_i} - \frac{2}{3} \frac{\partial V_p}{\partial X_p} \delta_{ik} \right) \right] \right\}}_{\Upsilon_{ij}}, \end{aligned} \quad (7)$$

where the operator  $\frac{d}{dt} (\equiv \frac{\partial}{\partial t} + V_k \frac{\partial}{\partial X_k})$  stands for the substantial derivative, which represents the rate of change following a fluid element.

The first term on the right-hand side of Eq. (7) is the self-deformation term, and it depends on the local state of the

velocity gradient tensor itself. On the other hand, the third term ( $\Upsilon_{ij}$ ) on right-hand side of Eq. (7) represents viscous action on the evolution of  $A_{ij}$ . The middle term of Eq. (7) is the pressure Hessian tensor ( $P_{ij}$ ). In incompressible turbulence, the evolution of  $P_{ij}$  is entirely dictated by velocity gradient and its higher derivatives. On the other hand, evolution of pressure Hessian in compressible flow fields depends on continuity as well as energy equations.

Suman and Girimaji [24] derived the exact evolution equation for  $P_{ij}$  in compressible flow as

$$\begin{aligned} \frac{dP_{ij}}{dt} = & \underbrace{-A_{kj}P_{ik} - A_{ki}P_{kj} - (n-1)A_{kk}P_{ij}}_{(I)} \\ & - \underbrace{\frac{n}{\rho} \left( \frac{\partial A_{kk}}{\partial X_j} \frac{\partial p}{\partial X_i} + \frac{\partial A_{kk}}{\partial X_i} \frac{\partial p}{\partial X_j} \right)}_{(II)} - \underbrace{\frac{1}{\rho} \frac{\partial A_{ki}}{\partial X_j} \frac{\partial p}{\partial X_k}}_{(III)} \\ & - \underbrace{\frac{np}{\rho} \frac{\partial^2 A_{kk}}{\partial X_i \partial X_j}}_{(IV)} + \underbrace{\frac{1}{\rho} \frac{\partial A_{kk}}{\partial X_j} \frac{\partial p}{\partial X_i} + \frac{np}{\rho^2} \frac{\partial A_{kk}}{\partial X_i} \frac{\partial \rho}{\partial X_j}}_{(V)} \\ & + \underbrace{\frac{n-1}{R} \frac{\partial}{\partial X_j} \left[ \frac{1}{\rho} \frac{\partial^2}{\partial X_i \partial X_k} \left\{ \kappa \frac{\partial}{\partial X_k} \left( \frac{p}{\rho} \right) \right\} \right]}_{(VI)} \\ & + \underbrace{(n-1) \frac{\partial}{\partial X_j} \left[ \frac{1}{\rho} \frac{\partial \sigma_{km}}{\partial X_i} A_{km} + \frac{1}{\rho} \sigma_{km} \frac{\partial A_{km}}{\partial X_i} \right]}_{(VII)}. \quad (8) \end{aligned}$$

In Eq. (8), the first term on its right-hand side represents the local interactions of velocity gradient and pressure Hessian. Terms II, III, IV, and V represent the interactions of pressure and inertial effects, and terms VI and VII represent conduction and viscous heating effects, respectively. Note that terms II–VII are nonlocal in nature, because they involve gradients or higher gradients of  $A_{ij}$  and  $P_{ij}$ . Further details on the significance of these terms can be found in Danish *et al.* [25].

### A. Quantities of interest

The evolution equation of  $A_{ij}$ , Eq. (7), can be decomposed into its symmetric and antisymmetric parts. The symmetric part gives the evolution equation of strain-rate tensor ( $S_{ij}$ ), while the antisymmetric part gives the evolution equation for rotation-rate tensor ( $W_{ij}$ ):

$$\frac{dS_{ij}}{dt} = -S_{ik}S_{kj} - W_{ik}W_{kj} - 0.5(P_{ij} + P_{ji}) + 0.5(\Upsilon_{ij} + \Upsilon_{ji}), \quad (9)$$

$$\frac{dW_{ij}}{dt} = -S_{ik}W_{kj} - W_{ik}S_{kj} - 0.5(P_{ij} - P_{ji}) + 0.5(\Upsilon_{ij} - \Upsilon_{ji}), \quad (10)$$

where

$$S_{ij} = \frac{1}{2}(A_{ij} + A_{ji}), \quad W_{ij} = \frac{1}{2}(A_{ij} - A_{ji}). \quad (11)$$

Using Eq. (10), we can write the equation for the magnitude of vorticity vector ( $\omega_i = -\epsilon_{ijk}W_{jk}$ , where  $\epsilon_{ijk}$  is the Levi-Civita

tensor) as [39]

$$\frac{d}{dt}(\omega_i \omega_i) = S_{ik}\omega_k \omega_i - 2\epsilon_{ijk}\tilde{P}_{jk}\omega_i + 2\epsilon_{ijk}\tilde{\Upsilon}_{jk}\omega_i, \quad (12)$$

where

$$\tilde{P}_{ij} = \frac{1}{2}(P_{ij} - P_{ji}), \quad \tilde{\Upsilon}_{ij} = \frac{1}{2}(\Upsilon_{ij} - \Upsilon_{ji}). \quad (13)$$

The first term on the right-hand side of Eq. (12) represents vortex-stretching mechanism [40]. The influence of strain-rate on vortex-stretching can be better explained with reference to the principal coordinate system of the local strain-rate tensor [41]:

$$S_{ik}\omega_k \omega_i = \omega_k \omega_k \lambda_i \cos^2(\hat{e}_\omega, \hat{e}_i), \quad (14)$$

where  $\lambda_i$  and  $\hat{e}_i$  are eigenvalues and eigenvectors of strain-rate tensor, respectively, and  $\hat{e}_\omega$  is the unit vorticity vector. In this work, we refer to  $\lambda_1$ ,  $\lambda_2$ , and  $\lambda_3$  as  $\alpha$ ,  $\beta$ , and  $\gamma$ , respectively, where  $\alpha > \beta > \gamma$ . Accordingly, the eigenvectors corresponding to these eigenvalues are represented by  $\hat{e}_\alpha$ ,  $\hat{e}_\beta$ , and  $\hat{e}_\gamma$ .

It is plausible to expect that a fluid particle, which is under an intense vortex-stretching process, will tend to become thinner in the  $\alpha$  direction. Consequently, the moment of inertia of the fluid particle would decrease along this direction. Assuming angular momentum of the chosen particle to be conserved, the reduction in moment of inertia would lead to an enhanced vorticity alignment along the  $\alpha$  eigenvector ( $\hat{e}_\alpha$ ). However, on the contrary, Ashurst *et al.* [2] demonstrated that, in incompressible turbulence, the instantaneous vorticity shows a strong tendency to align along the intermediate eigenvector ( $\hat{e}_\beta$ ) of strain rate but not along  $\hat{e}_\alpha$ . The explanation of the observed disparity seen in single-time Eulerian statistics of the alignment between  $\hat{e}_\omega$  and  $\hat{e}_\alpha$  and the expected behavior of  $\hat{e}_\omega$  to align with  $\hat{e}_\alpha$  has been provided recently by Xu *et al.* [33]. These authors used Lagrangian-based experiments rather than focusing solely on single-time Eulerian statistics and examined the Lagrangian statistics of the cosine of the angle between the instantaneous vorticity vector of a fluid element with the direction of the  $\alpha$  eigenvector of the same particle, which was labeled at some reference time  $t_{\text{ref}}$ . Subsequently, the average of the cosines for many such labeled fluid particles are obtained:

$$\langle [\hat{e}_i(t_{\text{ref}}) \cdot \hat{e}_\omega(t_{\text{ref}} + t)]^2 \rangle, \quad (15)$$

where  $\langle \cdot \rangle$  implies average over all the labeled fluid particles.

Using the experimental data of incompressible turbulence, Xu *et al.* [33] made the observation that  $\langle [\hat{e}_\alpha(t_{\text{ref}}) \cdot \hat{e}_\omega(t_{\text{ref}} + t)]^2 \rangle$  starts with a value of 1/3 at  $t_{\text{ref}}$ . This indicates no preferential alignment of vorticity with the largest eigenvector ( $\hat{e}_\alpha$ ). However with time, the correlation  $\langle [\hat{e}_\alpha(t_{\text{ref}}) \cdot \hat{e}_\omega(t_{\text{ref}} + t)]^2 \rangle$  increases and reaches its peak, which clearly indicates the enhanced tendency of instantaneous vorticity [ $\hat{e}_\omega(t_{\text{ref}} + t)$ ] to align with the  $\hat{e}_\alpha$  of reference time. Similar observations from DNS-based Lagrangian statistics of incompressible stationary isotropic turbulence have been reported by Chevillard and Meneveau [42] as well. The distinct behavior of vorticity to align with the  $\hat{e}_\alpha(t_{\text{ref}})$  is called the pirouette effect of turbulence [33].

It should be noted that the role of compressibility on Lagrangian statistics of vorticity vector alignment (how the

instantaneous vorticity vector responds to the reference principal coordinate system of strain-rate tensor) has not been explored before. In compressible flows, nonzero dilatation leads to decoupling of the three instantaneous principal strain-rate eigenvalues, which, in turn, leads to an additional degree of freedom. While for a volume-preserving fluid element, contraction in two principal directions guarantees expansion in the third direction, for an expanding or a contracting fluid element deformation in the third direction is not necessarily constrained by the deformation pattern in the first two principal directions. Therefore, it is of fundamental interest to investigate how this “new” degree of freedom in compressible turbulence affects the inertia tensor and in turn the dynamics of the vorticity vector itself.

Thus, in this paper, our interest is to examine and understand how compressibility modifies the Lagrangian statistics of the alignment between vorticity and the largest eigenvector of the strain-rate tensor. To facilitate this study, we first identify relevant compressibility parameters, which we shall use in Secs. V and VI, to isolate and understand the influence of compressibility on the pirouette effect of turbulence.

### B. Compressibility parameters

Isolating and understanding different aspects of compressible turbulence may need different compressibility parameters. Lee *et al.* [9], Suman and Girimaji [24,38], and Vaghefi and Madnia [43] have used  $a_{ii}$  (normalized dilatation) as a parameter to study the influence of compressibility on velocity gradients. Similarly,  $\delta$  (growth rate of dilatation) has been employed by Suman and Girimaji [10] to study the influence of compressibility on the pressure Hessian tensor. The flow-field topology has been recently used as a compressibility parameter by Danish *et al.* [44] in the study of compressible mixing. In the present work, we employ turbulent Mach number ( $M_t$ ), normalized dilatation ( $a_{ii}$ ), and topology ( $\Gamma$ ) as compressibility parameters to study the effects of compressibility on the pirouette effect in compressible turbulence. These compressibility parameters are defined as follows.

The turbulent Mach number ( $M_t$ ) is defined as

$$M_t = \sqrt{\frac{2K}{nR\bar{T}}}, \quad (16)$$

where  $K$ ,  $n$ ,  $R$ , and  $\bar{T}$  represent turbulent kinetic energy, specific-heat ratio, gas constant, and volume-averaged temperature, respectively. The turbulent Mach number is a statistical measure of acoustic to inertial timescale in the flow field.

The normalized dilatation ( $a_{ii}$ ) is defined as the trace of the normalized velocity gradient tensor ( $a_{ij}$ ), where

$$a_{ij} = \frac{A_{ij}}{\sqrt{A_{mn}A_{mn}}}. \quad (17)$$

The normalization of velocity gradient tensor ensures that its each component remains bounded within the interval  $[-1, 1]$ , and the trace of  $a_{ij}$  (normalized dilatation) is mathematically bounded between  $-\sqrt{3}$  and  $\sqrt{3}$  [38]. Locally normalized dilatation is a measure of rate of change in density of a local fluid element. Our third compressibility parameter is local flow

topology ( $\Gamma$ ). A detailed description of flow topology can be found in Suman and Girimaji [38] and Chong *et al.* [45]. Here, we provide just a brief summary.

### 1. Flow-field topology

Flow-field topology represents local instantaneous streamline patterns around an infinitesimal fluid particle observed with respect to a nonrotating reference frame translating with the fluid element. The patterns of streamline with respect to such a reference frame depend essentially on the nature of eigenvalues (real and complex) of velocity gradient tensor.

Chong *et al.* [45] showed that various possible topologies in a flow field can be easily presented on  $p$ - $q$ - $r$  space, where  $p$ ,  $q$ , and  $r$  are first, second, and third invariants of  $a_{ij}$ :

$$\begin{aligned} p &= -a_{ii}, \quad q = \frac{1}{2}(p^2 - a_{ij}a_{ji}), \text{ and} \\ r &= \frac{1}{3}(-p^3 + 3pq - a_{ij}a_{jk}a_{ki}). \end{aligned} \quad (18)$$

On the  $p$ - $q$ - $r$  space, the regions of real and complex eigenvalues of  $a_{ij}$  are separated by a surface  $S$ :

$$S \equiv 27r^2 + (4p^3 - 18pq)r + (4q^3 - p^2q^2) = 0. \quad (19)$$

The surface  $S$  is further split into two surfaces,  $S1a$  and  $S1b$ , which osculate each other at the origin:

$$S1a \equiv \frac{1}{3}p(q - \frac{2}{9}p^2) - \frac{2}{27}(-3q + p^2)^{3/2} - r = 0, \quad (20)$$

$$S1b \equiv \frac{1}{3}p(q - \frac{2}{9}p^2) + \frac{2}{27}(-3q + p^2)^{3/2} - r = 0. \quad (21)$$

The region of complex eigenvalues has another partitioning surface  $S2$ . The surface  $S2$ , which contains only imaginary eigenvalues, is given by

$$S2 \equiv pq - r = 0. \quad (22)$$

Based on the values of  $p$ ,  $q$ ,  $r$ , and the surface  $S2$ , various flow topologies can be identified. A list of all possible topologies is presented in Table I.

TABLE I. Zones of various topologies on  $p$ - $q$ - $r$  space, where acronyms are: stable-focus-stretching (SFS), unstable-focus-compressing (UFC), unstable-node/saddle/saddle (UNSS), stable-node/saddle/saddle (SNSS), unstable-focus-stretching (UFS), unstable-node/unstable-node/unstable-node (UN/UN/UN), stable-focus-compressing (SFC), stable-node/stable-node/stable-node (SN/SN/SN).

Acronyms	$p = 0$	$p < 0$	$p > 0$
SFS	$r < 0$	$r < 0$ and $S2 > 0$	$r < 0$
UFC	$r > 0$	$r > 0$	$r > 0$ and $S2 < 0$
UNSS	$r > 0$ and $q < 0$	$r > 0$	$r > 0$ and $q < 0$
SNSS	$r < 0$ and $q < 0$	$r < 0$ and $q < 0$	$r < 0$
UFS		$r < 0$ and $S2 < 0$	
UN/UN/UN		$r < 0$ and $q > 0$	
SFC			$r > 0$ and $S2 > 0$
SN/SN/SN			$q > 0$ and $r > 0$

**III. DESCRIPTION OF DIRECT NUMERICAL SIMULATIONS**

We employ direct numerical simulations of compressible decaying isotropic turbulence for this study. These simulations are performed using a solver based on the gas kinetic method (GKM). The GKM has emerged as a viable tool for performing DNS simulations of compressible turbulence. The method was originally proposed by Xu and Prendergast [46], who demonstrated its capability in simulating laminar compressible flows. The GKM scheme has been shown to demonstrate numerical stability and a superior shock capturing ability. Unlike Riemann solvers [47,48], the gas kinetic method uses Boltzmann equation to construct fluxes of macroscopic governing equations. Over the past few years, several studies have been reported wherein the credibility of GKM-based solvers has been very well demonstrated in simulating compressible turbulent flows as well [49–51].

Our DNS simulations are performed over a cubic domain of size  $2\pi$  with  $256^3$  uniformly spaced grid points. Periodic boundary conditions are imposed on the opposite sides of the cube. The gas is assumed to be calorically perfect. The initial velocity field is generated in physical space using a uniform random number generator. After transforming the velocity field in Fourier space, the condition of incompressibility is imposed. Subsequently, we impose the desired energy spectrum [52]:

$$E(\kappa) = A_0 \kappa^4 \exp(-2\kappa^2/\kappa_0^2), \quad (23)$$

where  $\kappa$  is wave number and the values for spectrum constants  $A_0$  and  $\kappa_0$  are taken 0.011 and 4, respectively [52]. Finally, we transform back the velocity field in the physical space.

In this work, we use two sets of compressible simulations that have the same initial conditions except turbulent Mach number (simulations A and B in Table II). For simulation A the value of  $M_t$  is 0.488 and for simulation B its value is taken as 0.3.

Note that we have taken care to ensure that all our numerical simulations are well resolved temporally as well as spatially. In Fig. 1(a), we present the evolution of velocity derivative skewness for  $A_{11}$ ,  $A_{22}$ , and  $A_{33}$  obtained from simulation A. After an initial dip, the skewness of velocity derivatives are observed to attain a value in the range  $[-0.5, -0.4]$ . As Lee *et al.* [53] demonstrated that the velocity derivative skewness attains a value in the range  $[-0.5, -0.4]$  in a physically realistic turbulent flow field. Thus, the result shown in Fig. 1(a) clearly indicates that the simulation cases presented in this work have reached a state of realistic turbulence for  $t/\tau_{\lambda_0} > 1$ , where

TABLE II. Initial parameters for DNS simulations.  $Re_\lambda = \sqrt{\frac{20}{3\epsilon\nu}}K$  represents Reynolds number, where  $K$ ,  $\epsilon$ , and  $\nu$  are turbulent kinetic energy, its dissipation rate, and kinematic viscosity, respectively.

Simulation	$Re_\lambda$	$M_t$	Grid size	$A_0$	$\kappa_0$
A	175	0.488	$256^3$	0.011	4
B	175	0.3	$256^3$	0.011	4
C	175	Incompressible	$256^3$	0.011	4

$\tau_{\lambda_0}$  represents eddy turnover time based on initial root-mean square velocity ( $u'_0$ ) and Taylor microscale ( $\lambda_0$ ),

$$\tau_{\lambda_0} = \frac{\lambda_0}{u'_0}. \quad (24)$$

To assess the reliability of the present solver, we have compared our results with the DNS results of Samtaney *et al.* [52]. In their work, the authors [52] used a 10<sup>th</sup> order accurate Padé method to perform DNS of compressible decaying turbulence. Owing to the high order used by Samtaney *et al.* [52], their DNS results can be considered as a validation reference for other compressible turbulence solver over similar range of  $M_t$  and  $Re_\lambda$  [54].

In Figs. 1(b)–1(d), we present the evolutions of normalized dissipation-rate ( $\epsilon/\epsilon_0$ ),  $M_t$ , and  $Re_\lambda$  from simulation A (solid lines) and from case D9 of Samtaney *et al.* [52] (symbol  $\circ$ ). Note that the initial conditions for simulation A have been carefully matched with those of D9. From Figs. 1(b)–1(d) we see that the agreement between simulation A and D9 of Samtaney *et al.* [52] are excellent. We have also validated our GKM-based DNS solver with cases D4 and D6 of Samtaney *et al.* [52]. Again the agreement was found to be excellent (figures not shown). Based on these observations we conclude that our GKM-based solver is capable of reliably simulating compressible decaying turbulence over the range of Mach number and Reynolds number considered in this work.

To contrast the effect of compressibility on Lagrangian statistics, if any, we also present results from incompressible turbulence. Our DNS solver for incompressible decaying turbulence employs 6<sup>th</sup> order compact finite difference method. The incompressible code has been extensively validated by Manu [55]. Like compressible simulations (A and B), we use the same initial spectrum, spectrum constants, and  $Re_\lambda$  for simulation C as well (Table II).

**IV. LAGRANGIAN PARTICLE TRACKER**

The GKM solver finds numerical solution of partial differential equations that govern velocity and other thermodynamic variables in the Eulerian framework, wherein the spatial variable  $\mathbf{X}$  and time  $t$  are independent variables. However, to study the Lagrangian dynamics of flow field, one needs to find the evolution history of various flow quantities following a fluid particle. Thus, extraction of Lagrangian statistics necessitates the development of a post-processing algorithm (a Lagrangian particle tracker), which takes the Eulerian field data at successive time instants as input and tracks the trajectory of a chosen fluid particle. Subsequent to tracking, such an algorithm must also accurately interpolate the flow quantities of interest associated with the chosen fluid particle at all later time instants.

The trajectory of a fluid particle ( $\mathbf{X}^+(\mathbf{y}, t)$ ) can be tracked by integrating its equation of motion [56]:

$$\frac{\partial \mathbf{X}^+(\mathbf{y}, t)}{\partial t} = \mathbf{V}(\mathbf{X}^+(\mathbf{y}, t), t), \quad (25)$$

where superscript “+” represents a Lagrangian flow variable, and  $\mathbf{y}$  indicates the label or identifier assigned to the fluid particle. Following Yeung and Pope [56], we use initial

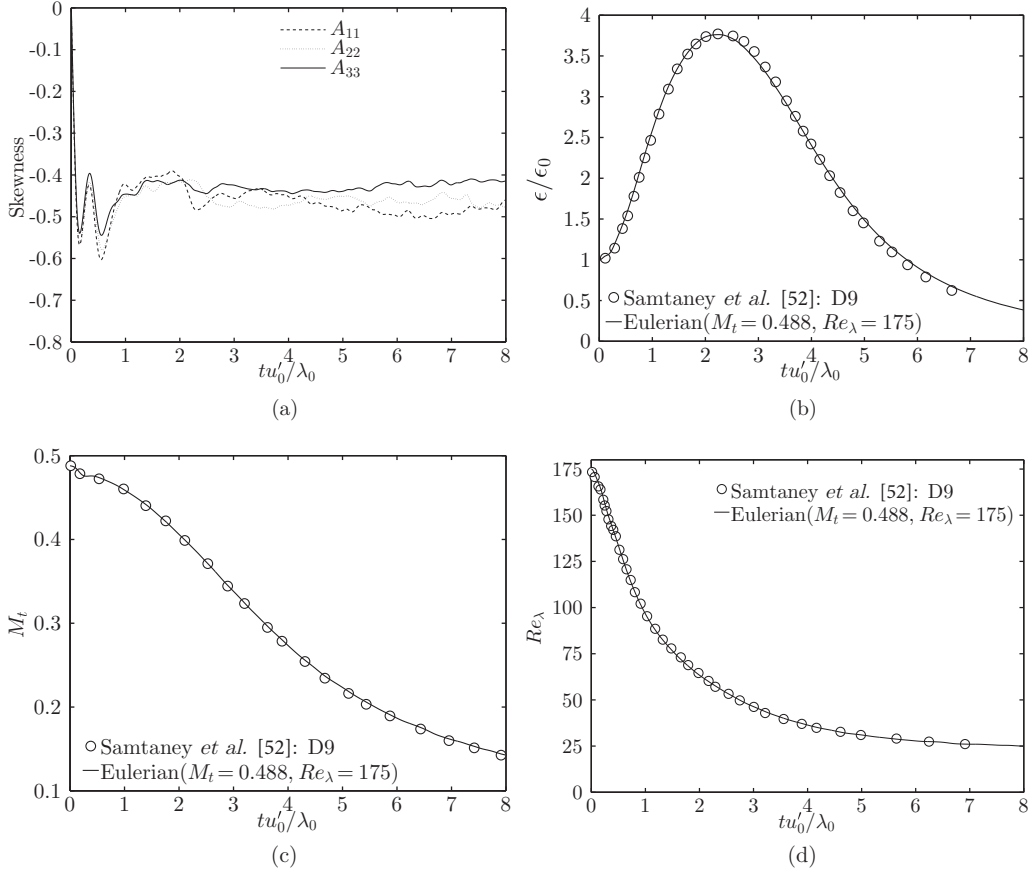


FIG. 1. Time evolution of (a) velocity-derivative skewness, (b) dissipation rate, (c) Mach number, and (d) Reynolds number with initial  $M_t = 0.488$ ,  $Re_\lambda = 175$  (simulation A). The symbols  $\lambda_0$  and  $u_0'$  represent Taylor microscale and root-mean-square velocity based on initial conditions.

positions of fluid particles as their labels:

$$\mathbf{y} = \mathbf{X}(t = 0). \quad (26)$$

In conjunction with the Eulerian DNS dataset, the equation of motion, Eq. (25), can be numerically integrated to compute the location of labeled particles at subsequent time instants. Since the Eulerian fields of velocity and other flow variables are already spatially discretized and the same is available only at discretized time instants, in general, the location of a chosen fluid particle at the next time instant may not coincide with the grid points of the computational domain. Therefore, an accurate interpolation method is required by any Lagrangian particle tracker. Yeung and Pope [56] examined various interpolation methods for their study of incompressible turbulence and found the performance of the interpolation method based on cubic splines to be the most satisfactory. In this work, too, we employ a cubic-splines-based interpolator. For performing the numerical integration of Eq. (25) we employ the second-order Runge-Kutta method.

Employing an LPT for a compressible turbulent flow field poses additional challenge as compared to incompressible turbulence. This is because of the presence of shocklets, which induce steep gradients in all flow variables. Our LPT has been particularly validated to ensure that it performs with a satisfactory level of accuracy even in compressible turbulence.

In Fig. 2 we present the pdf of local Mach number obtained from simulation A at time  $t = 1.56\tau$ , where  $\tau = 0.667$  [52]. The local Mach number ( $M_{loc}$ ) is defined as

$$M_{loc} = (V_i V_i / c^2)^{1/2}, \quad (27)$$

where  $c$  is local sonic speed. In Fig. 2, the dashed line shows the pdf of  $M_{loc}$  obtained using  $256^3$  data points of

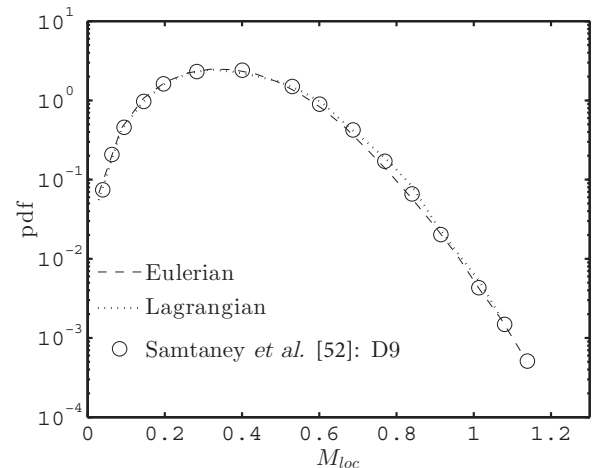


FIG. 2. Pdf of local Mach number ( $M_{loc}$ ) from simulation A at time  $t/\tau = 1.56$ , where  $\tau = 0.667$  [52].

Eulerian single-time statistics. On the other hand, the dotted lines represent the pdf obtained from a sample of 10 000 fluid particles that have been identified initially and tracked subsequently using the LPT from time  $t = 0$  to  $t = 1.56\tau$ . This can be called Lagrangian single-time statistics. Clearly, the agreement between Eulerian single-time statistics and Lagrangian single-time statistics is excellent, indicating the tracking and interpolation related calculations employed by LPT are accurate enough. On this figure we have also presented results from Samtaney *et al.* [52] (symbol  $\circ$ ). Clearly, our results show excellent agreement with that reported by Samtaney *et al.* [52]. Based on the validations presented in Figs. 1 and 2, we conclude that our Eulerian DNS database and Lagrangian particle tracker are reliable enough to be used to isolate and study the role of compressibility on the Lagrangian statistics of vorticity–strain-rate alignment dynamics, Eq. (15). The results of this study are presented in Secs. V and VI. Our convergence study (results not presented) shows that a sample size of 10 000 particles is adequate for computing unconditional Lagrangian statistics, whereas a sample size of 30 000 particles is found to be adequate for accurately computing the Lagrangian statistics conditioned on normalized dilatation and topology.

## V. INFLUENCE OF MACH NUMBER

In Fig. 3, we present the alignment correlations of vorticity vector with the  $\alpha$ -eigenvector of strain-rate tensor from simulations A, B, and C (Table II). Note that the quantity  $\langle [\hat{e}_\alpha(t_{\text{ref}}) \cdot \hat{e}_\omega(t_{\text{ref}} + t)]^2 \rangle$  assuming a value: (i)  $1/3$  implies no preferential alignment tendency between the two vectors, (ii) lower than  $1/3$  implies the tendency of the two vectors to align perpendicular to each other, and (iii) more than  $1/3$  is indicative of the tendency of the two vectors to align parallel to each other [33].

We start our discussion with Fig. 3(a), wherein we show the evolution of  $\langle [\hat{e}_\alpha(t_{\text{ref}}) \cdot \hat{e}_\omega(t_{\text{ref}} + t)]^2 \rangle$  with  $t_{\text{ref}} = 1.4\tau_{\lambda_0}$ . In all these simulation cases the evolution starts with somewhat different values, however, all these values are below  $1/3$ , indicating the presence of some fluid elements which have the two vectors possibly aligned perpendicular to each other. The evolution of  $\langle [\hat{e}_\alpha(t_{\text{ref}}) \cdot \hat{e}_\omega(t_{\text{ref}} + t)]^2 \rangle$  in all three simulations first follows a monotonic increase and thereafter decays slowly and appears to be settling down to a value of  $1/3$ . The initial monotonic increase lasts for about  $0.2\tau_{\lambda_0}$  and in the later phase the correlation attains a value close to  $1/3$  over a time period of about one  $\tau_{\lambda_0}$ . This common trend seen in the three simulation cases clearly demonstrates that just like the behavior seen

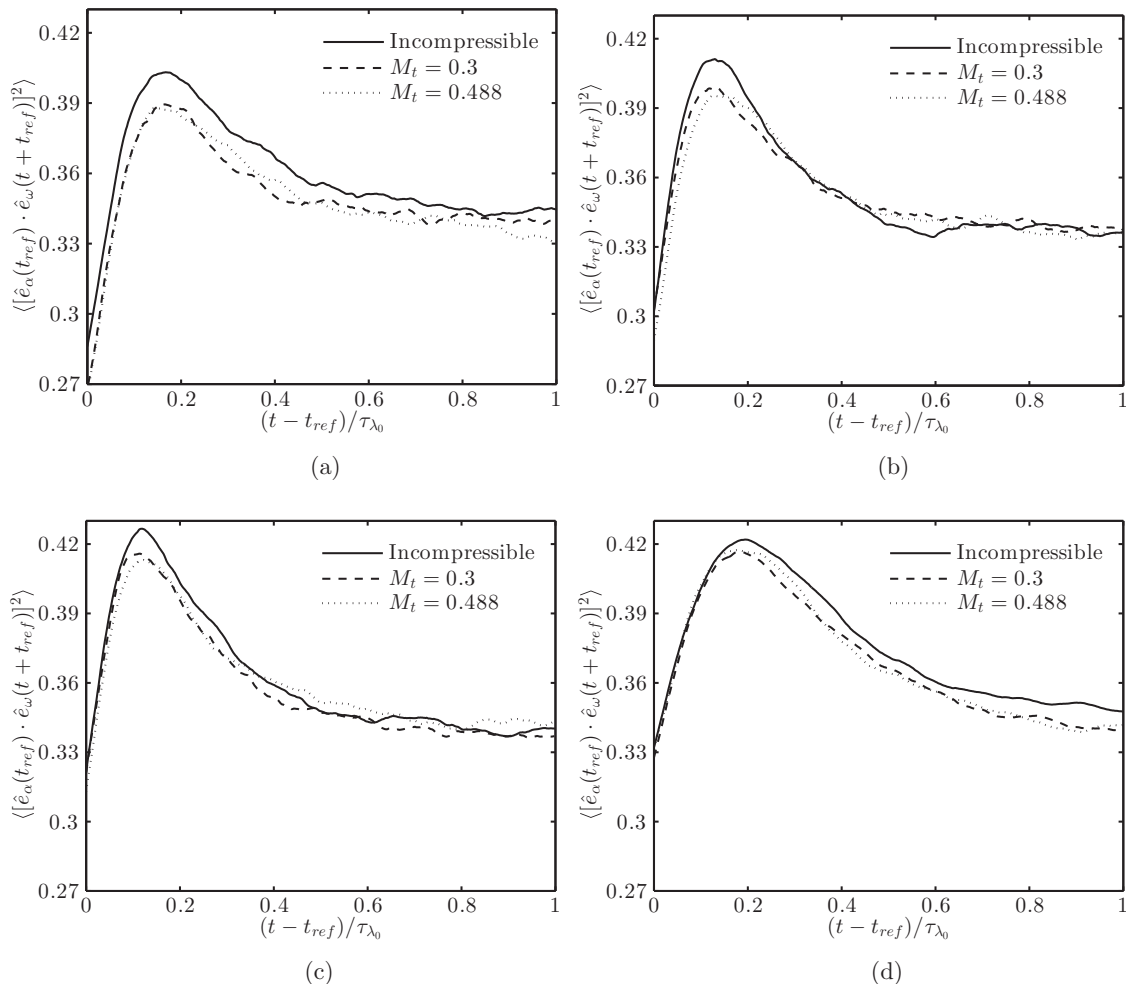


FIG. 3. Alignment of vorticity with  $\alpha$ - eigenvector of strain-rate at reference times (a)  $1.4\tau_{\lambda_0}$ , (b)  $2.1\tau_{\lambda_0}$ , (c)  $2.8\tau_{\lambda_0}$  and (d)  $5.0\tau_{\lambda_0}$  from simulations A, B, and C (Table II).

in incompressible turbulence (simulation C and observations made by Xu *et al.* [33] and Chevillard and Meneveau [42]), in compressible turbulence too the vorticity vector shows a distinct tendency to align with the initial direction of the largest strain rate eigenvector ( $\hat{e}_\alpha$ ) over a time interval of about  $0.2\tau_{\lambda_0}$ . The subsequent decay to a value of  $1/3$  indicates that in the second stage of evolution the orientation preferences are gradually weakened and eventually lost by the end of one  $\tau_{\lambda_0}$ . Despite these similarities, however, the peak values in compressible cases (A and B) are smaller than that in incompressible turbulence. Thus, we infer that compressibility seems to weaken the tendency of the two vectors to align with each other. In Figs. 3(b)–3(d), we plot the evolution of  $\langle [\hat{e}_\alpha(t_{\text{ref}}) \cdot \hat{e}_\omega(t_{\text{ref}} + t)]^2 \rangle_\Gamma$  from the same three simulations (A, B, and C) but with different  $t_{\text{ref}}$ . In each figure all three simulations show the same two stage evolution—sharp increase in the first stage of evolution and subsequently a decay to a value of  $1/3$ . However, we observe that the differences between the evolutions in compressible and incompressible cases seem to reduce as the chosen reference time increases. In Fig. 3(d), wherein  $t_{\text{ref}}$  has been chosen to have a very high value of  $5\tau_{\lambda_0}$ , the compressible and incompressible evolutions are almost identical, indicating the negligible influence of compressibility on the tendency of vorticity to align with the largest initial strain-rate eigenvector. To further understand and explain the behavior seen in Figs. 3(a)–3(d), in the next section we focus on one of these compressible simulation cases (case A) and further examine the vorticity alignment statistics as functions of (i) local normalized dilatation ( $a_{ii}$ ) and (ii) local flow topology ( $\Gamma$ ).

## VI. INFLUENCE OF TOPOLOGY AND NORMALIZED DILATATION

In this section we first consider Lagrangian statistics conditioned on topology in incompressible turbulence itself. In light of this discussion, subsequently in Sec. VI B, we examine how topology as well as dilatation influence the Lagrangian statistics of  $\langle [\hat{e}_\alpha(t_{\text{ref}}) \cdot \hat{e}_\omega(t_{\text{ref}} + t)]^2 \rangle$  in compressible turbulence.

### A. Influence of topology in incompressible turbulence

Figure 4 shows the evolution of  $\langle [\hat{e}_\alpha(t_{\text{ref}}) \cdot \hat{e}_\omega(t_{\text{ref}} + t)]^2 \rangle$  conditioned upon initial ( $t - t_{\text{ref}} = 0$ ) local topology ( $\Gamma = \text{UNSS, SNSS, SFS, and UFC}$ ) with  $t_{\text{ref}} = 2.1\tau_{\lambda_0}$ . All results are from simulation C (incompressible turbulence). Note that previous studies, investigating one-time unconditional statistics of vorticity alignment, do not show any significant preference of vorticity to align with the  $\alpha$  eigenvector (for example, Fig. 6 in Ashurst *et al.* [2]). This behavior can be traced in Fig. 3(b), where the curve representing the unconditioned statistics in incompressible turbulence (solid line) shows a value close to  $0.33$  at  $t - t_{\text{ref}} = 0$ . However, when the incompressible behavior is separately conditioned on topology ( $\Gamma$ ), significant influence of topology can be seen on the value of  $\langle [\hat{e}_\alpha(t_{\text{ref}}) \cdot \hat{e}_\omega(t_{\text{ref}} + t)]^2 \rangle_\Gamma$  at  $t - t_{\text{ref}} = 0$  itself (Fig. 4). The SFS topology shows a higher value of  $\langle [\hat{e}_\alpha(t_{\text{ref}}) \cdot \hat{e}_\omega(t_{\text{ref}} + t)]^2 \rangle_\Gamma$  at  $t - t_{\text{ref}} = 0$ , indicating that even initially ( $t - t_{\text{ref}} = 0$ ), the fluid elements with SFS topology already have vorticity better aligned with the  $\alpha$  eigenvector

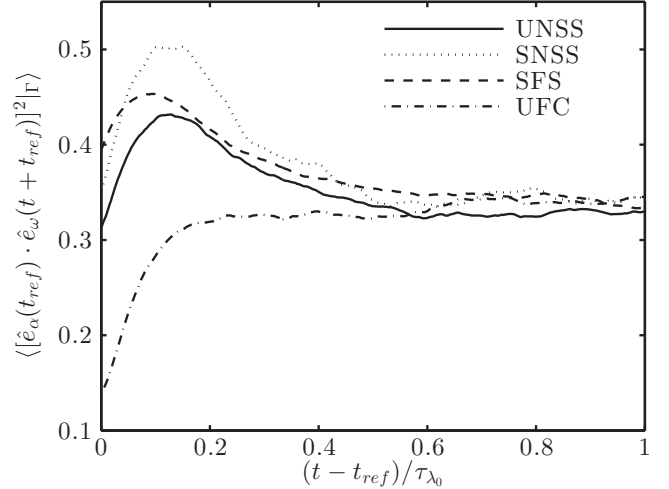


FIG. 4. Alignment of instantaneous vorticity and  $\hat{e}_\alpha$  with  $t_{\text{ref}} = 2.1\tau_{\lambda_0}$  conditioned on topology ( $\Gamma$ ) from incompressible simulation (case C).

than the fluid elements associated with other topologies. While initial values of UNSS and SNSS do not show any preferential alignment at  $t - t_{\text{ref}} = 0$ , UFC shows a distinct tendency of vorticity and  $\alpha$  eigenvector to be mutually perpendicular to each other.

In Table III, we show the percentage population of each of the four topologies in simulation C at  $t - t_{\text{ref}} = 0$  (similar results reported earlier by Suman and Girimaji [38]). From Table III, we observe that at  $t - t_{\text{ref}} = 0$ , topology SFS has the highest population, which is closely followed by UNSS and UFC, whereas SNSS forms just about 9% of the total population. We further observe that the population of SFS, UNSS, and SNSS add up to approximately 75%, whereas UFC is almost 25%. Thus the population-weighted average of  $\langle [\hat{e}_\alpha(t_{\text{ref}}) \cdot \hat{e}_\omega(t_{\text{ref}} + t)]^2 \rangle$  can be expected to be close to  $0.33$ —which explains why the unconditional alignment of vorticity and  $\alpha$  eigenvector at  $t - t_{\text{ref}} = 0$  does not show any preferential alignment tendency, whatsoever.

Next we examine the evolution of  $\langle [\hat{e}_\alpha(t_{\text{ref}}) \cdot \hat{e}_\omega(t_{\text{ref}} + t)]^2 \rangle_\Gamma$  over a time interval of one  $\tau_{\lambda_0}$  (Fig. 4). All four curves show strong tendency to increase over a time interval of about  $0.2\tau_{\lambda_0}$ . UNSS, SNSS, and SFS topologies show a distinct tendency of the vorticity vector to align with the initial  $\alpha$  eigenvector, with the highest tendency seen in SNSS topology followed by SFS and UNSS. During the same time, however, in UFC topology, pirouette effect completely nullifies the initial orthogonal orientation of the vorticity vector with the initial  $\alpha$  eigenvector. Even though SNSS seems to be the most conducive to allowing vorticity to align with the  $\alpha$  eigenvector, its contribution toward the overall unconditional statistics is rendered limited by its smaller population in the flow field.

TABLE III. Percentage population of various topologies in incompressible turbulence.

Flow field	UNSS	SNSS	SFS	UFC
Incompressible (case C)	30.77	8.94	35.61	24.67

On the other hand, SFS and UNSS with its considerably high alignment tendency combined with its high population is clearly the main contributor toward shaping the unconditioned behavior of  $\langle [\hat{e}_\alpha(t_{\text{ref}}) \cdot \hat{e}_\omega(t_{\text{ref}} + t)]^2 \rangle$  as seen in previous studies of incompressible turbulence [33,42].

Thus the major conclusions that we draw from this study are: (i) even though at a given time, unconditional statistics of alignment between the vorticity vector and the  $\alpha$  eigenvector has been previously found to be random, our study reveals that the conditional tendency of  $\langle [\hat{e}_\alpha(t_{\text{ref}}) \cdot \hat{e}_\omega(t_{\text{ref}} + t)]^2 | \Gamma \rangle$  is considerably high in SFS, and in contrast considerably low in UFC; (ii) at later times the tendency of the SNSS topology to align the vorticity vector with the initial  $\alpha$  eigenvector is the highest among all topologies, followed by that of SFS and UNSS. However, owing to their significantly higher population, SFS and UNSS topology seem to be responsible for shaping the previously observed [33,42] overall unconditional tendency of the vorticity vector to align with the initial  $\alpha$  eigenvector in incompressible turbulence.

### B. Influence of topology and dilatation in compressible turbulence

In this section we examine the role of dilatation ( $a_{ii}$ ) and topology ( $\Gamma$ ) in shaping the Lagrangian dynamics of the vorticity–strain-rate alignment in compressible turbulence. Results from simulation A (Table II) with  $t_{\text{ref}} = 2.1\tau_{\lambda_0}$  are employed for this examination. In Figs. 5(a)–5(e), the alignment correlations conditioned jointly on initial topology and dilatation with  $t_{\text{ref}} = 2.1\tau_{\lambda_0}$  are presented separately for each topology. In each subfigure, the Lagrangian evolution is shown separately for initially positive ( $a_{ii} > 0$ ), negative ( $a_{ii} < 0$ ), and negligibly-small ( $|a_{ii}| \approx 0$ ) dilatation values. Note that UFS exists only at  $a_{ii} > 0$  and SFC exists only at  $a_{ii} < 0$ . Plots for these two topologies (SFC and UFS) are shown in Fig. 5(c).

We start our discussion with UNSS topology [Fig. 5(a)]. All evolutions ( $a_{ii} > 0$ ,  $a_{ii} < 0$ , and  $a_{ii} \approx 0$ ) start with an initial value of  $1/3$ —implying no preferential alignment tendency at  $t - t_{\text{ref}} = 0$ . However, they all show enhanced alignment over  $0.2\tau_{\lambda_0}$  and subsequently decorrelate. Notably, no significant influence of dilatation is observed. Similarly, in Fig. 5(b), which shows statistics conditioned upon UFC topology, no significant influence of dilatation is seen. Furthermore, the behavior at  $a_{ii} > 0$ ,  $a_{ii} < 0$ , and  $a_{ii} \approx 0$  for both UNSS and UFC are almost the same as what is seen in incompressible turbulence (simulation C, Fig. 4).

In Fig. 5(c) we present conditional statistics of UFS and SFC topologies. UFS and SFC are two “new” topologies that exist only in compressible flow field. UFS exists only at positive dilatations, whereas SFC exists only at negative dilatations. Both these topologies start with an initial tendency of vorticity vector to be aligned perpendicular to the  $\alpha$  eigenvector. However, subsequently this tendency is weakened leading to a statistically random state.

In contrast to UNSS and UFC [Figs. 5(a) and 5(b)], SNSS and SFS [Figs. 5(d) and 5(e)] topologies seem to show significant influence of initial normalized dilatation. While the initially expanding ( $a_{ii} > 0$ ) and contracting ( $a_{ii} < 0$ ) fluid particles with SFS topology show almost the same behavior as

seen in incompressible turbulence (simulation C, Fig. 4), the fluid elements with initially negligible  $a_{ii}$  exhibit considerably different evolution than what is seen in incompressible turbulence. A similar trend is observed for SNSS topology except for its contracting particles, which seem to lie between expanding and zero dilatation particles. However, for both of these topologies (SNSS and SFS), the fluid elements with initially negligible normalized dilatation show a considerably reduced tendency of the vorticity vector to align with the initial direction of the  $\alpha$  eigenvector. Based on this observation, we now attempt to explain the overall unconditional statistics of vorticity and  $\alpha$ -eigenvector alignment tendency seen earlier in Fig. 3.

Since UNSS and UFC do not show any departure from their behavior seen in incompressible turbulence [Figs. 4, 5(a), and 5(b)], it is plausible to conclude that these topologies do not have any role in modifying the unconditioned behavior of  $\langle [\hat{e}_\alpha(t_{\text{ref}}) \cdot \hat{e}_\omega(t_{\text{ref}} + t)]^2 \rangle$  in compressible turbulence (Fig. 3). The new topologies UFS and SFC, on the other hand, do not show any distinct enhanced tendency to align the vorticity with initial direction of  $\alpha$  eigenvector, and since they are nonexistent in the incompressible case (simulation C) their presence can potentially weaken the alignment tendency of vorticity vector and  $\alpha$  eigenvector in compressible turbulence. However, their population percentage is small (approximately 7%, see Table IV), and thus their influence on the unconditional statistics of Fig. 3 is expected to be limited. The major topologies responsible for reducing the pirouette effect in compressible turbulence seem to be SFS and SNSS associated with those fluid elements having initially negligible dilatation ( $a_{ii} \approx 0$ ). This is because the values of  $\langle [\hat{e}_\alpha(t_{\text{ref}}) \cdot \hat{e}_\omega(t_{\text{ref}} + t)]^2 |_{a_{ii} \approx 0, \Gamma = \text{SNSS}} \rangle$  [solid line in Fig. 5(d)] and  $\langle [\hat{e}_\alpha(t_{\text{ref}}) \cdot \hat{e}_\omega(t_{\text{ref}} + t)]^2 |_{a_{ii} \approx 0, \Gamma = \text{SFS}} \rangle$  [solid line in Fig. 5(e)] are significantly less than their corresponding values in incompressible turbulence. Note that among SFS and SNSS topologies, the percentage population at zero dilatation (Table IV) for SFS is quite significant (approximately 40%), whereas the population of SNSS is very small (approximately 8%).

In Table V, we also show the percentage population of fluid particles which have positive, negative, and zero dilatations from simulation A at  $t - t_{\text{ref}} = 0$ . We observe that the fluid particles having zero dilatation at  $t_{\text{ref}}$  constitute almost one-third of the total population. Thus, based on our analysis and discussion, we conclude that the moderating influence of compressibility on the pirouette effect in compressible turbulence is due to the substantial reduction of  $\langle [\hat{e}_\alpha(t_{\text{ref}}) \cdot \hat{e}_\omega(t_{\text{ref}} + t)]^2 \rangle$  of those fluid elements that have  $a_{ii} \approx 0$  and SFS topology at  $t = t_{\text{ref}}$ .

## VII. MODELING IMPLICATIONS

As discussed in Sec. II, the velocity gradient evolves under the influence of three different mechanisms: self-deformation of velocity gradient, pressure Hessian, and viscous action. From the Lagrangian point of view, the pressure Hessian and viscous terms are unclosed, and thus they need to be modeled. In the past, several studies have been performed wherein the central focus was to develop Lagrangian models for velocity-gradient evolution equation [16,18,20–25]. For

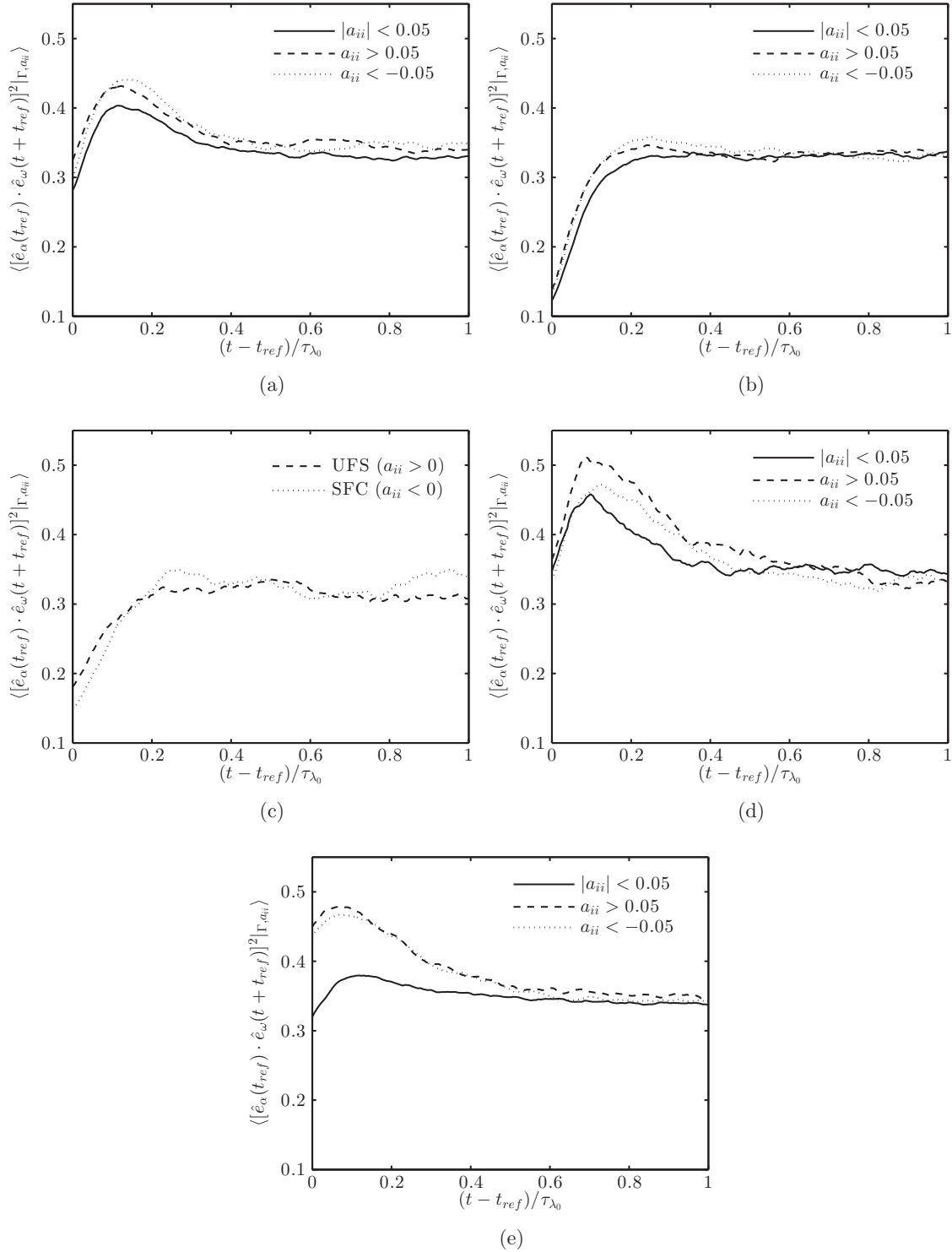


FIG. 5. Alignment correlations conditioned on dilatation and topology obtained from simulation A using  $t_{ref} = 2.1\tau_{\lambda_0}$ . (a) UNSS, (b) UFC, (c) UFS/SFC, (d) SNSS, and (e) SFS.

incompressible turbulence, the state-of-the-art model is due to Chevillard *et al.* [22]; which is commonly known as recent-fluid-deformation-closure (RFD) model.

In compressible turbulence, the modeling task is more complicated as compared to incompressible turbulence because of the following two reasons: (a) the pressure Hessian behaves as an autonomous quantity that is governed by its

own evolution equation, and (b) in the limit of low Mach number (incompressible limit) the model should relax to the strictly incompressible case. The first model for compressible turbulence was proposed by Suman and Girimaji [23,24], which was further improved by Danish *et al.* [25].

In the past, typically, the credibility of such Lagrangian models—for both incompressible and compressible

TABLE IV. Percentage population of various topologies available at zero, positive, and negative dilatations from simulation A at  $t_{\text{ref}} = 2.1\tau_{\lambda_0}$ .

Dilatation-sign	UNSS	SNSS	SFS	UFC	UFS	SFC
Zero ( $ a_{ii}  < 0.05$ )	28.85	7.71	39.88	23.56		
Positive ( $a_{ii} \geq 0.05$ )	34.45	6.21	29.92	21.89	7.50	
Negative ( $a_{ii} \leq -0.05$ )	23.18	15.59	31.42	22.91		6.88

turbulence—are established by comparing their performance with DNS (Eulerian) results, like alignment of vorticity with instantaneous strain-rate and pressure Hessian eigenvectors, symmetric and nonsymmetric pressure Hessian, etc. [1,25]. Since the nature of these models is inherently Lagrangian, a legitimate test of their performance would be to compare model results directly with the Lagrangian results. The recent finding of the pirouette effect has provided an excellent test bed to assess the potential of such a model with reference to the Lagrangian statistics. Chevillard and Meneveau [42] showed that the model based on the RFD approach very well recovers the pirouette effect of turbulence; however, the model lacks in capturing the alignment tendency of vorticity vector with the eigenvectors of pressure Hessian tensor. Thus, the model based on RFD has a scope of improvement in terms of pressure Hessian tensor. Similarly, the results of the present work can also be leveraged to assess and improve the existing Lagrangian models of velocity-gradient tensor for incompressible as well as compressible turbulence.

Unlike incompressible turbulence, the antisymmetric portion of the pressure Hessian tensor in a compressible flow field is nonzero, which in turn influences the dynamics of vorticity Eq. (12). Our results from this study show that the conditional statistics of vorticity dynamics are influenced directly by local topology and normalized dilatation. Thus, it is plausible to infer that prospective modeling conjectures for the topology- and dilatation-conditioned pressure Hessian behavior may prove to be more successful than the usual approach of modeling the unconditional form of the tensor directly as done in previous works [24]. Relevant examples of such a “conditional” modeling strategy are the works done by Wilczek and Meneveau [39] and by the authors [44] in modeling unclosed scalar-gradient–velocity-gradient interactions in compressible turbulence. However, details regarding similar modeling proposals for the pressure Hessian tensor in compressible turbulence require further research and are not the focus of this paper.

TABLE V. Percentage population of fluid particles which have zero, positive, and negative dilatations from simulation A at  $t_{\text{ref}} = 2.1\tau_{\lambda_0}$ .

$a_{ii}$	Percentage population
Zero ( $ a_{ii}  < 0.05$ )	37.57
Positive ( $a_{ii} \geq 0.05$ )	32.28
Negative ( $a_{ii} \leq -0.05$ )	30.14

VIII. CONCLUSIONS

With the motivation to understand the influence of compressibility on vorticity dynamics and its interactions with the strain-rate tensor, in this work, we specifically investigate the so-called pirouette effect of turbulence (Lagrangian evolution of the alignment between instantaneous vorticity vector and the initial direction of the largest strain-rate eigenvector). We perform the study by using direct numerical simulation results of compressible decaying isotropic turbulence. To extract the relevant Lagrangian statistics, we employ a cubic-spline-based Lagrangian particle tracker in conjunction with “almost” time-continuous DNS datasets. Lagrangian statistics of vorticity alignment with the initially largest strain-rate eigenvector obtained from two different compressible simulations are presented. These two compressible simulations differ only in terms of initial turbulent Mach number. Results from incompressible turbulence are also included to contrast and clearly identify the differences between incompressible and compressible turbulent flow fields.

We find that, like in incompressible turbulence, the vorticity shows a distinct tendency to align with the initial direction of the largest strain-rate eigenvector. However, the extent of this alignment tendency seems to be weaker in compressible turbulence as compared to incompressible flow. To further understand the reasons behind this moderating effect of compressibility, we examine the Lagrangian statistics of the alignment between the instantaneous vorticity vector and the initial strain-rate eigenvector conditioned upon local flow field topology and normalized dilatation. Toward this goal, we first examine the influence of topology on alignment statistics in incompressible turbulence itself, and thereafter leverage this understanding to develop better insight into compressible turbulence.

For incompressible turbulence, the conditional alignment statistics exhibit a strong influence of topology. Among the possible topologies (UNSS, SNSS, SFS, and UFC) in incompressible turbulence, the topology SNSS is observed to be associated with the strongest tendency of the vorticity vector to align with the initially largest strain-rate eigenvector followed by SFS and UNSS topologies. On the other hand, the topology UFC shows a distinctly different alignment tendency, where the vorticity is found to be oriented perpendicular to the initially largest strain-rate eigenvector.

Upon performing a similar analysis on alignment tendency of compressible turbulence, we find that the alignment tendency is not only affected by topology but also by normalized dilatation. Fluid elements when categorized based on the initial state of dilatation,  $a_{ii} > 0$ ,  $a_{ii} < 0$ ,  $a_{ii} \approx 0$ , demonstrate that while the initially expanding ( $a_{ii} > 0$ ) and contracting ( $a_{ii} < 0$ ) fluid elements for a given topology have almost identical alignment tendency as seen in incompressible turbulence, the fluid elements with initially small dilatation ( $a_{ii} \approx 0$ ) show significant differences. These differences are most pronounced in SFS and SNSS topologies. In fluid elements with initial  $a_{ii} \approx 0$ , both these topologies show a substantially weaker tendency for vorticity to align with the largest eigenvector. However, the percentage populations of SFS and SNSS at zero dilatation indicate that the contribution from SNSS would be

very small as compared to SFS. Thus, based on our study, we conclude that the presence of fluid elements with initial  $a_{ii} \approx 0$  and SFS topology are responsible for the overall moderation of the alignment tendency of the vorticity vector in compressible turbulence.

### ACKNOWLEDGMENTS

The authors acknowledge the financial support provided by the Aeronautical Research & Development Board, India, and the computational support provided by the High Performance Computing facility of IIT Delhi for this work.

- 
- [1] C. Meneveau, *Annu. Rev. Fluid Mech.* **43**, 219 (2011).
- [2] W. T. Ashurst, A. R. Kerstein, R. M. Kerr, and C. H. Gibson, *Phys. Fluids* **30**, 2343 (1987).
- [3] A. Tsinober, E. Kit, and T. Dracos, *J. Fluid Mech.* **242**, 169 (1992).
- [4] L. K. Su and W. J. A. Dahm, *Phys. Fluids* **8**, 1883 (1996).
- [5] J. Martín, A. Ooi, M. Chong, and J. Soria, *Phys. Fluids* **10**, 2336 (1998).
- [6] N. Mordant, P. Metz, O. Michel, and J.-F. Pinton, *Phys. Rev. Lett.* **87**, 214501 (2001).
- [7] F. van der Bos, B. Tao, C. Meneveau, and J. Katz, *Phys. Fluids* **14**, 2456 (2002).
- [8] B. Lüthi, A. Tsinober, and W. Kinzelbach, *J. Fluid Mech.* **528**, 87 (2005).
- [9] K. Lee, S. S. Girimaji, and J. Kerimo, *J. Turbul.* **10**, 1 (2009).
- [10] S. Suman and S. S. Girimaji, *Phys. Fluids* **25**, 125103 (2013).
- [11] G. I. Taylor, *Proc. Lond. Math. Soc* **s2-20**, 196 (1922).
- [12] L. F. Richardson, *Proc. R. Soc. Lond. A Mat.* **110**, 709 (1926).
- [13] G. Falkovich, K. Gawędzki, and M. Vergassola, *Rev. Mod. Phys.* **73**, 913 (2001).
- [14] S. B. Pope, *Annu. Rev. Fluid Mech.* **26**, 23 (1994).
- [15] S. B. Pope, *Phys. Fluids* **14**, 1696 (2002).
- [16] P. Vieillefosse, *J. Phys.* **43**, 837 (1982).
- [17] B. J. Cantwell, *Phys. Fluids A* **4**, 782 (1992).
- [18] S. S. Girimaji and C. G. Speziale, *Phys. Fluids* **7**, 1438 (1995).
- [19] M. Chertkov, A. Pumir, and B. I. Shraiman, *Phys. Fluids* **11**, 2394 (1999).
- [20] E. Jeong and S. S. Girimaji, *Theor. Comp. Fluid Dyn.* **16**, 421 (2003).
- [21] L. Chevillard and C. Meneveau, *Phys. Rev. Lett.* **97**, 174501 (2006).
- [22] L. Chevillard, C. Meneveau, L. Biferale, and F. Toschi, *Phys. Fluids* **20**, 101504 (2008).
- [23] S. Suman and S. S. Girimaji, *J. Fluid Mech.* **620**, 177 (2009).
- [24] S. Suman and S. S. Girimaji, *J. Fluid Mech.* **683**, 289 (2011).
- [25] M. Danish, S. Suman, and B. Srinivasan, *Phys. Fluids* **26**, 126103 (2014).
- [26] P. K. Yeung and S. B. Pope, *J. Fluid Mech.* **207**, 531 (1989).
- [27] P. K. Yeung, *J. Fluid Mech.* **427**, 241 (2001).
- [28] H. Yu and C. Meneveau, *Phys. Rev. Lett.* **104**, 084502 (2010).
- [29] H. Yu, K. Kanov, E. Perlman, J. Graham, E. Frederix, R. Burns, A. Szalay, G. Eyink, and C. Meneveau, *J. Turbul.* **13**, 1 (2012).
- [30] A. La Porta, G. A. Voth, A. M. Crawford, J. Alexander, and E. Bodenschatz, *Nature* **409**, 1017 (2001).
- [31] S. Ott and J. Mann, *J. Fluid Mech.* **422**, 207 (2000).
- [32] G. A. Voth, A. La Porta, A. M. Crawford, J. Alexander, and E. Bodenschatz, *J. Fluid Mech.* **469**, 121 (2002).
- [33] H. Xu, A. Pumir, and E. Bodenschatz, *Nature Phys.* **7**, 709 (2011).
- [34] C. Beetz, C. Schwarz, J. Dreher, and R. Grauer, *Phys. Lett. A* **372**, 3037 (2008).
- [35] C. Schwarz, C. Beetz, J. Dreher, and R. Grauer, *Phys. Lett. A* **374**, 1039 (2010).
- [36] Y. Yang, J. Wang, Y. Shi, Z. Xiao, X. T. He, and S. Chen, *Phys. Rev. Lett.* **110**, 064503 (2013).
- [37] Y. Yang, J. Wang, Y. Shi, Z. Xiao, X. T. He, and S. Chen, *J. Fluid Mech.* **786**, R6 (2016).
- [38] S. Suman and S. S. Girimaji, *J. Turbul.* **11**, 1 (2010).
- [39] M. Wilczek and C. Meneveau, *J. Fluid Mech.* **756**, 191 (2014).
- [40] A. Tsinober, *An Informal Introduction to Turbulence*, Vol. 63 (Springer Science & Business Media, Berlin, 2001).
- [41] J. Wang, Y. Shi, L.-P. Wang, Z. Xiao, X. T. He, and S. Chen, *J. Fluid Mech.* **713**, 588 (2012).
- [42] L. Chevillard and C. Meneveau, *Phys. Fluids* **23**, 101704 (2011).
- [43] N. S. Vaghefi and C. K. Madnia, *J. Fluid Mech.* **774**, 67 (2015).
- [44] M. Danish, S. Suman, and S. S. Girimaji, *J. Fluid Mech.* **793**, 633 (2016).
- [45] M. S. Chong, A. E. Perry, and B. J. Cantwell, *Phys. Fluids A* **2**, 765 (1990).
- [46] K. Xu and K. H. Prendergast, *J. Comput. Phys.* **114**, 9 (1994).
- [47] P. L. Roe, *J. Comput. Phys.* **43**, 357 (1981).
- [48] M.-S. Liou and C. J. Steffen, *J. Comput. Phys.* **107**, 23 (1993).
- [49] J. Kerimo and S. S. Girimaji, *J. Turbul.* **8**, 1 (2007).
- [50] W. Liao, Y. Peng, and L.-S. Luo, *Phys. Rev. E* **80**, 046702 (2009).
- [51] G. Kumar, S. S. Girimaji, and J. Kerimo, *J. Comput. Phys.* **234**, 499 (2013).
- [52] R. Samtaney, D. I. Pullin, and B. Kosovic, *Phys. Fluids* **13**, 1415 (2001).
- [53] S. Lee, S. K. Lele, and P. Moin, *Phys. Fluids A* **3**, 657 (1991).
- [54] B. Srinivasan, The BGK and LRS Schemes for Computing Euler and Navier-Stokes Flows, PhD. thesis, Stanford University, 2005.
- [55] C. Manu, Analysis of ILES Capabilities in Capturing Turbulent Flows, Master's thesis, IIT Delhi, 2014.
- [56] P. K. Yeung and S. B. Pope, *J. Comput. Phys.* **79**, 373 (1988).